Photocycloaddition Reaction of Atropisomeric Maleimides: Mechanism and Selectivity

Xue-Ping Chang,[a] Yiying Zheng,[b] Ganglong Cui,*[a] Wei-Hai Fang[a] and Walter Thiel*[b]

We report a density functional study on the mechanism of the [2+2] photocyclization of atropisomeric maleimides. Experimentally, the reaction is known to proceed through the triplet state. We have located all relevant S_0 and T_1 minima and transition states, as well as the T_1/S_0 crossing points, and mapped eight stepwise photocyclization pathways for four different conformers in the T_1 state that lead to distinct regioisomers. In the preferred four pathways (one for each conformer) the initially formed C-C bond involves the terminal carbon atom of the alkene moiety. This regioselectivity originates from electrostatic preferences (arising from the charge distribution in the polarized C=C double bonds) and from the different thermodynamic stability of the resulting triplet diradical intermediates (caused by electron donation effects that stabilize the radical centers). The formation of the second C-C bond is blocked in the T_1 state by prohibitively high barriers and thus occurs after intersystem crossing to the ground state. Furthermore, we rationalize substitution effects on enantioselectivity and diastereoselectivity and identify their origin.

Introduction

Asymmetric synthesis, also called chiral or enantioselective synthesis, is one of the cornerstones of modern chemistry. It is particularly important in the field of chemical and pharmaceutical industry, because different enantiomers or diastereomers of a molecule usually have distinct chemical and biological activities.[1–5] Conventional chiral synthesis has evolved to such an extent that chemo-, regio-, and stereo-control can be readily achieved in thermal reactions within complex, templated, and multifunctional molecules.[6–13]

Asymmetric photochemical transformations have not reached the same level of success, even though they may provide complementary access to molecules with unique stereochemical and structural complexity.[14–18] Reaction control is more difficult in synthetic photochemistry because the basic bond-forming and bond-breaking steps are often governed by the lifetime of a key excited state, the formation of which may be dominated by complex photophysical processes in the molecule (e.g. internal conversion and intersystem crossing) and affected by its complicated surroundings. Asymmetric photoreactions are generally fast processes so that the desired excited-state reactivity and product stereochemistry must be manipulated within the short lifetime of the excited species.[19,20] These requirements may be alleviated to some extent by performing photoreactions in confined media, in supramolecular templates, and in the solid state,[21–27] but it is still a challenge to control the stereoselectivity of photoreactions in solution.

Recently, Sivaguru and co-workers employed atropisomeric compounds[28–31] to achieve a variety of asymmetric photochemical transformations in solution, including 6π, 4π, and Norrish-Yang photocyclizations, photocycloadditions, and Paterno-Büchi reactions.[32–40] In these studies, they managed to transfer axial chirality in the reactants to point chirality in the products upon irradiation. In 2014, they broadened the scope of this strategy to visible-light induced [2+2] photocycloaddition of atropisomeric maleimides, achieving high enantioselectivity (*ee* > 98%), high diastereoselectivity (exo/endo selectivity, *dr* > 99%), and exclusive chemoselectivity.[40] Photocycloaddition was observed under direct irradiation, triplet-sensitized ultraviolet irradiation, and metal-free catalyzed visible-light irradiation.[40] The enantioselectivity and diastereoselectivity was found to be largely dependent on the substituents at the maleimide double bond, while being only minimally affected by the substituents at the alkenyl tether.[40] The observed exo/endo photoproduct selectivity and the chiral transfer during the reaction in the triplet excited state were explained by a plausible two-step photocatalytic mechanism, which is schematically shown in Fig. 1.

Irradiation of the reactant maleimide (**1**) in the presence of a sensitizer provides access to the triplet state and leads to the formation of 1,4-diradical intermediates (DR1-DR4); in a second step, these triplet diradicals undergo intersystem crossing (ISC) to the singlet state, and the resulting singlet diradicals recombine and cyclize to yield the major exo-product (**2**) and the minor endo product (**3**).[40] In this scenario, there are several issues that call for further clarification at the atomistic level, for example: What are the energy profiles associated with the proposed reaction paths? Where do the triplet diradical intermediates return to the singlet ground state? What is the origin of exo/endo photoproduct and path selectivity? Why is intermediate DR1 more favorable than DR2 in the exo photoaddition? Why are only the substituents on the maleimide double bond crucial for the observed diastereoselectivity? It is clearly difficult to resolve these microscopic issues solely by experimental means, and it is thus desirable to address them through high-level electronic structure calculations.

[a] *Key Laboratory of Theoretical and Computational Photochemistry, Ministry of Education, College of Chemistry, Beijing Normal University, Beijing 100875, China*
[b] *Max-Planck-Institut für Kohlenforschung, Kaiser-Wilhelm-Platz 1, 45470 Mlheim an der Ruhr, Germany*

† Electronic Supplementary Information (ESI) available: Figures and Tables as well as Cartesian coordinates. See DOI: 10.1039/x0xx00000x

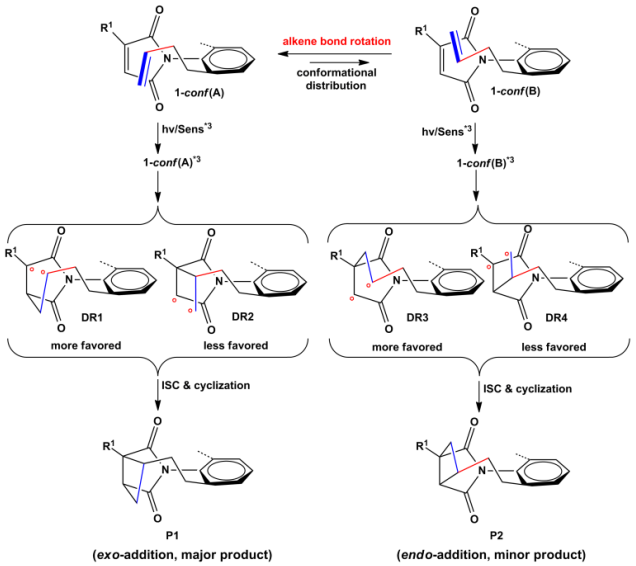

Fig. 1 Intramolecular [2+2] *exo/endo* photocycloaddition reactions of atropisomeric maleimides in the presence of a sensitizer. Adapted from Scheme 5 of the work of Kumarasamy et al.[40]

Such computational studies on mechanism and selectivity are abundantly available for ground-state thermal reactions (for selected recent reviews see refs. 41–46), but much less so for photoreactions. In this article, we report the first computational investigation on the mechanism of the novel [2+2] photocyclization reactions[40] using density functional theory (DFT). We first focus on the substrate with a methyl substituent on the maleimide (R^1=Me in Fig. 1, substrate **1i** in the experimental work[40]), for which we present and discuss eight stepwise reaction pathways (one major and one minor path for each of the four conformers considered) that lead to distinct photoproducts. Thereafter we elucidate the origin of enantioselectivity and diastereoselectivity in this reaction as well as the role of the substituents on the maleimide double bond and the alkenyl tether.

Computational Methods

DFT Calculations

Minima and transition states in the T_1 and S_0 states were optimized using the unrestricted DFT method[47] with the B3LYP,[48–51] M06-2X,[52,53] PBE0,[53] and CAM-B3LYP[54] exchange correlation functionals, in combination with the all-electron 6-31G* basis set.[55,56] The nature of all these stationary points on the potential energy surfaces was confirmed by computing their harmonic vibrational frequencies. The polarizable continuum model (PCM) was employed to implicitly account for solvent effects (acetonitrile).[57] Grimme-type dispersion corrections (D3) were included throughout.[58] Gibbs free energies of all optimized structures were calculated at 298.15 K and 1 atm. Singly-occupied molecular orbitals associated with triplet states were obtained through biorthogonalizing unrestricted molecular orbitals to maximally align electron pairs. All electronic structure calculations were carried out using the GAUSSIAN09 package.[59]

Crossing-Point Optimization

To optimize the T_1/S_0 crossing points, we adopted the penalty function method of Ciminelli et al.[60] as implemented in the DL-FIND module of the ChemShell-3.5 package.[61,62] The objective function is defined as

$$(R) = \frac{\mathrm{E}_I + \mathrm{E}_J}{2} + c_1 c_2^2 \, ln\left[1 + \left(\frac{\mathrm{E}_J - \mathrm{E}_I}{c_2}\right)^2\right]$$

where E_I and E_J denote the potential energies of the electronic states *I* and *J*. For the parameters c_1 and c_2, we used the recommended values of 5.0 $(\mathrm{kcal/mol})^{-1}$ and 5.0 kcal/mol, respectively. This optimization scheme for intersection structures has been shown to work well for large systems, in particular also in the condensed phase.[63,64]

Results

Scope of the Computational Study

Inspection of Fig. 1 would seem to suggest that it is sufficient to consider the two depicted conformers A and B. However, the alkenyl side chain of the reactant maleimide (**1**) may adopt different conformations, and the heterocycle and the aryl ring need not be oriented strictly perpendicular to each other but may have dihedral angles different from 90°. In a conformational search at the DFT level, we found four distinct local ground-state minima for the reactant maleimide (**1**) that have an orientation suitable for [2+2] photocycloaddition (see Table S1 of the Supporting Information). We will present computational results for all these four conformers (labeled as A–D) but will focus in the discussion on two prototypical conformers (A, B) for head-to-head and head-to-tail cycloaddition. The results for the two other conformers (C, D) are generally analogous and will thus mostly be given only as Supporting Information (SI).

Reactants in the S_0 and T_1 States

At the B3LYP-D3/6-31G*/PCM level, we optimized the two relevant S_0 reactant conformers A and B in acetonitrile solution, see Fig. 2. A and B (or C and D) can be inter-converted by rotation of the terminal alkene group around the neighboring C–C single bond, while A and C (or B and D) are related by rotation of the maleimide group around the N–C(aryl) bond. We note that A and D (or B and C) are not enantiomeric pairs because all four conformers have similar tilts between the heterocycle and the aryl ring (dihedral angles C5-N-C6-C9 of 110–114°) whereas the four corresponding enantiomers have opposite tilts (see Table S1 of the SI).

Structurally, the terminal alkene groups in A and B are all located reasonably close to the C3=C4 double bond of the maleimide group; for example, at the B3LYP-D3/6-31G*/PCM level, the C2-C3 and C1-C4 distances in A are computed to be 4.058 and 4.442 Å; the C1-C3 and C2-C4 distances in B are 4.753 and 4.636 Å. Energetically, conformer A is predicted to be the most stable species in the S_0 state at the B3LYP-D3/6-31G*/PCM level; however, it is only 0.5, 0.2, and 1.7 kcal/mol lower in energy than the other three conformers B, C, and D. Given the limited accuracy of DFT, all four conformers need to be considered when studying the photocyclization reaction.

In the presence of a photosensitizer, the photocyclization has been shown experimentally to involve the T_1 state.[40] The T_1 reactant conformers are thus important for understanding the mechanism. As in the case of the S_0 state, we obtained four stable conformers in the T_1 state, but again focus on the prototypical cases A and B (as shown in Fig. 2). Structurally, compared with their S_0 counterparts, the two C–C distances relevant to the photocyclization reaction change little for A, whereas they decrease by more than ca. 0.3 Å for B. Energetically, all four T_1 conformers are close to each other, within 0.5 kcal/mol at the B3LYP-D3/6-31G*/PCM level. They lie about 53 kcal/mol above their S_0 counterparts.

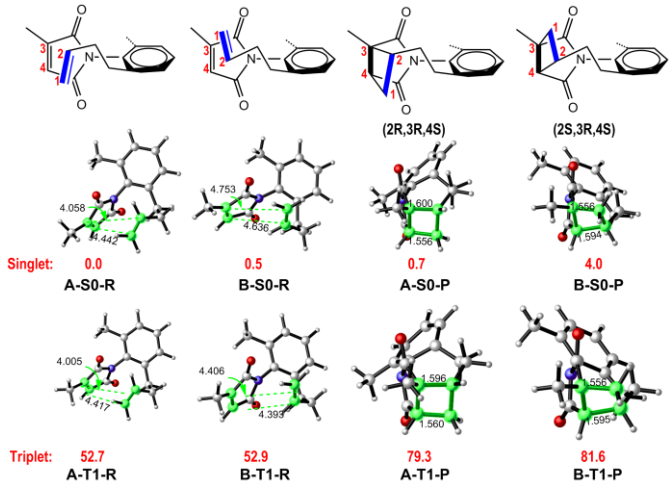

Fig. 2 Two S_0 and two T_1 reactant (left) and product (right) conformers optimized at the B3LYP-D3/6-31G*/PCM level. Also shown are the C-C distances (Å) related to the [2+2] photocyclization reaction (carbon atoms involved in green). The relative Gibbs free energies (kcal/mol) are given underneath the structures. See Supporting Information for Cartesian coordinates.

The T_1 state in the reactant region originates from a local ππ* electronic excitation within the maleimide group. In the Supporting Information, the left panel of Fig. S1 shows the two singly-occupied molecular orbitals (SOMOs) in the T_1 state of conformer A, which are both spatially localized within the maleimide moiety. One of them (top-left in ESI, Fig. S1) has a node in the middle of the C=C double bond of the maleimide group, indicating that the ππ* excitation leads to a breaking of the C=C double bond. This is reflected in the elongation of the corresponding C-C bond from 1.340 Å in the S_0 state to 1.475 Å in the T_1 state of conformer A. The electronic structure of the T_1 state in the other three conformers is analogous (B, C, and D; see Supporting Information).

As discussed above, conformer A can be converted to conformer C by rotation of the maleimide group around the N-C(aryl) bond. We identified approximate transition states for this process in the S_0 and T_1 states by computing the corresponding minimum-energy pathways (see Supporting Information). The conversion from A to C is quite difficult in both cases, with Gibbs free energy barriers of 33.8 kcal/mol in the S_0 state and 19.7 kcal/mol in the T_1 state at the B3LYP-D3/6-31G*/PCM level (see the left panel of Fig. 3). The barrier in the T_1 state is substantial, but lower than that in the S_0 state, which may be partly caused by the pyramidalization of the maleimide N atom. In contrast, the interconversion between A and B is much easier (see the right panel of Fig. 3), since the barrier that needs to be overcome is only 4.0 kcal/mol in the S_0 state and 4.3 kcal/mol in the T_1 state. In the course of this rotation, there exists a transient conformer, which however cannot undergo photocyclization because of the improper orientation of the terminal alkene group.

Products in the S_0 and T_1 States

[2+2] photocyclization of the two conformationally distinct conformers A and B will give rise to two distinct product conformers. Fig. 2 shows the corresponding S_0 and T_1 structures optimized at the B3LYP-D3/6-31G*/PCM level.

In each case, two single C-C bonds are formed: C1-C4 and C2-C3 for A; C1-C3 and C2-C4 for B. The products have typical bond lengths, for example, 1.556 and 1.600 Å for C1-C4 and C2-C3 in A, and 1.556 and 1.594 Å for C1-C3 and C2-C4 in B, respectively (see Fig. 2). Energetically, the A product is the most stable S_0 species (lying ca. 3 kcal/mol below the B product). Furthermore, the Gibbs free energies of the A product [A-S0-P] is only 0.7 kcal/mol higher than that of the A reactant [A-S0-R], while the corresponding free energy difference for B ([B-S0-P] versus [B-S0-R]) is somewhat higher (3.5 kcal/mol at the B3LYP-D3/6-31G*/PCM level).

Analogously, we also optimized the two T_1 products, as shown in Fig. 2. Their Gibbs free energies relative to the S_0 state of the A reactant [A-S0-R] lie in the range between 79–82 kcal/mol (B3LYP-D3/6-31G*/PCM) and are thus much higher than those of the T_1 reactants (on average 53 kcal/mol, see Fig. 2). These T_1 products are thus not accessible in the photoreaction (see ESI for further details).

T_1 Reaction Paths

Experimentally, there is a major and a minor reaction path in the [2+2] photocyclization of the maleimides leading to *exo* and *endo* products, respectively.[40] After initial excitation to the S_1 state, interactions with the photosentizer lead to fast energy transfer and decay to the lowest triplet state, and hence the photocyclization begins in the T_1 state. Thus, we examined a total of four T_1 paths (major and minor) for conformers A and B to understand the mechanism. Fig. 4 depicts these possible reaction paths. In the following we discuss them in more detail.

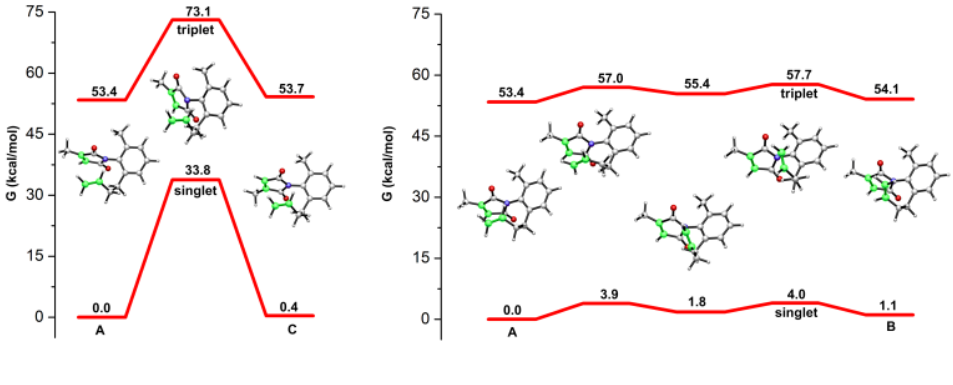

Fig. 3 Computed Gibbs free energy profiles (kcal/mol) in the S_0 and T_1 states (B3LYP-D3/6-31G*/PCM). Left, A-C interconversion by rotation around the N–C(aryl) bond; right, A-B interconversion by rotation of the terminal ethylene group around the neighboring C–C single bond. Only T_1 structures are shown. See text for discussion. Analogous calculations using the 6-31+G* basis with diffuse functions give very similar results (see Table S10 and Figure S16 in the Supporting Information).

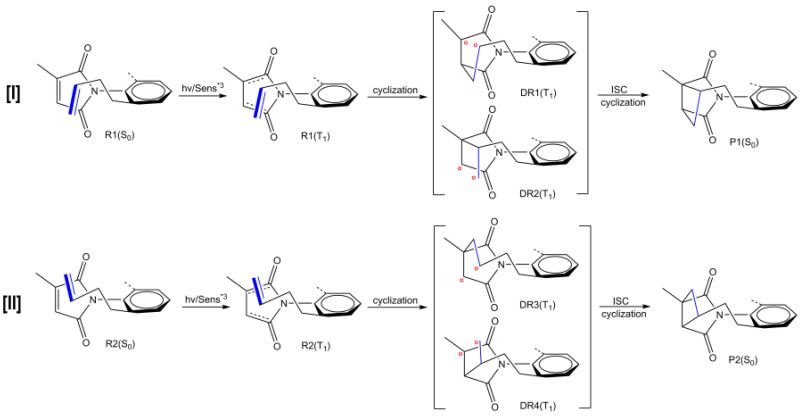

Fig. 4 Reaction paths for [2+2] photocyclization starting from the two reactant conformers.

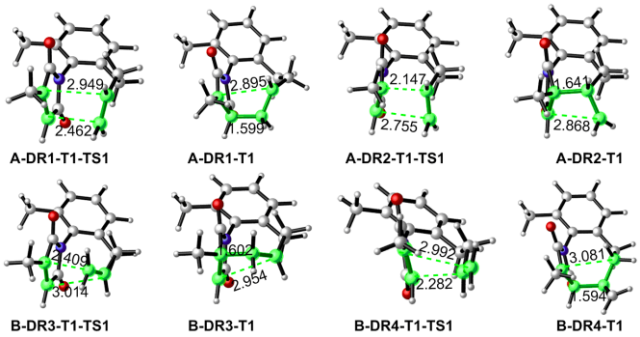

Fig. 5 Stationary-point structures on the T_1 pathways starting from the reactant conformers A and B computed at the B3LYP-D3/6-31G*/PCM level (SI for C and D). Also shown are the lengths (Å) of the two C-C bonds involved in the [2+2] photocyclization reaction (carbon atoms involved in green). See Supporting Information for Cartesian coordinates.

Starting from the A conformer [A-T1-R] the two paths available in the T_1 state are labeled as DR1 and DR2 in Fig. 6. In the former, the C1-C4 bond is formed first to yield in a diradical intermediate (A-DR1-T1 in Fig. 5); subsequent formation of the C2-C3 bond leads to ring closure. In the latter, the two C-C bonds are formed in the opposite sequence (first C2-C3, then C1-C4) via another diradical intermediate (A-DR2-T1). The structures of the transition states and intermediates for paths DR1 and DR2 are shown in Fig. 5.

In the first half reaction of path DR1, the C1-C4 distance changes from 4.417 Å in A-T1-R via 2.462 Å in A-DR1-T1-TS1 to 1.599 Å in A-DR1-T1. The corresponding Gibbs free energy barrier, relative to the triplet reactant A-T1-R, is computed to be 1.5 kcal/mol. The diradical intermediate A-DR1-T1 is predicted to be 12.6 kcal/mol lower in energy than A-T1-R. Thus, for DR1, the first half reaction is kinetically facile and thermodynamically favorable.

In path DR2, the C2-C3 bond is formed first, as can again be seen from the relevant C-C distances in the stationary points (Fig. 5). Mechanistically, this path is unimportant because the relevant Gibbs free energy barrier is much higher than its counterpart on path DR1: relative to the triplet reactant A-T1-R, it is computed to be 9.7 kcal/mol (vs. 1.5 kcal/mol in DR1; see above).

There are two analogous photocyclization paths for reactant conformer B in the T_1 state (B-T1-R), which are labeled as DR3 and DR4 in Fig. 6. In DR3, the initial formation of the C1-C3 bond is computed to be facile (Gibbs free energy barrier of 2.8 kcal/mol) and exergonic by 10.3 kcal/mol. In DR4, the first half reaction requires more activation (8.8 kcal/mol). Analogous results are obtained for the photocyclization reactions starting from the triplet reactants C-T1-R and D-T1-R (i.e. paths DR5, DR6, DR7, and DR8); they are presented and discussed in the Supporting Information (see ESI, Fig. S2 for the optimized structures).

According to our calculations, the second half reaction will not take place in any of the T_1 pathways (DR1-DR8), because the Gibbs free energy of each transition state is more than 40 kcal/mol higher than that of the corresponding reactant (Fig. S10, see Supporting Information for further details).

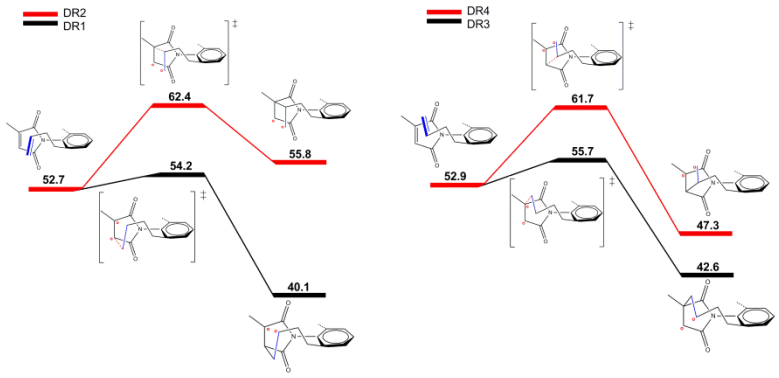

Fig. 6 Gibbs free energy profiles (in kcal/mol) for the [2+2] photocyclizations starting from the reactant conformers A and B computed at the B3LYP-D3/6-31G*/PCM level.

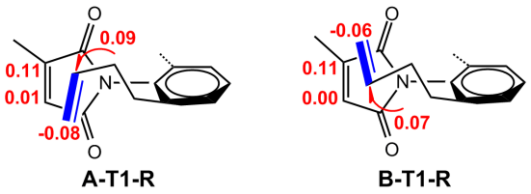

Fig. 7 Mulliken charges of the four carbon atoms involved in the [2+2] photoaddition reaction of the different triplet reactant conformers.

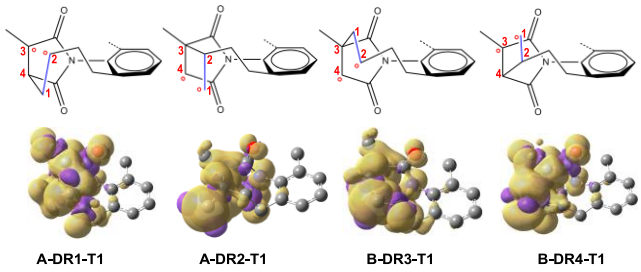

Fig. 8 Schematic drawings and spin-density plots of the four diradical intermediates A-DR1-T1, A-DR2-T1, B-DR3-T1, and B-DR4-T1. See text for discussion.

Our calculations thus predict that the formation of the first C-C bond is much easier when involving the terminal carbon atom of the alkene group (DR1 and DR3), rather than the other carbon atom (DR2 and DR4). For instance, the free energy barrier for the first half reaction is 1.5 kcal/mol for DR1 and 9.7 kcal/mol for DR2. This can be qualitatively understood as follows.

First, electrostatic interactions favor the preferred mode of attack. Fig. 7 depicts the T_1 Mulliken charges of the carbon atoms involved in the photoaddition reaction. Evidently, the terminal carbon atom of the alkene group (C1) is always negatively charged (-0.06 to -0.08) whereas the adjacent carbon atom (C2) carries an opposing positive charge (+0.07 to +0.09). In the maleimide double bond, the carbon atom with the methyl substituent (C3) is always positively charged (+0.11), whereas the neighboring carbon atom (C4) is essentially neutral (0.00 to 0.01). In the case of conformers B, attractive electrostatic interactions directly favor C1-C3 bond formation, whereas in the case of A, there are repulsive C2-C3 interactions that indirectly favor C1-C4 bond formation (Fig. 7).

Second, the relative stability of the diradical intermediates on paths DR1-DR4 may also play an important role for the path selectivity. For instance, A-DR1-T1 is 15.7 kcal/mol lower in energy than A-DR2-T1 (Fig. 6). This is related to the spatial distribution of the spin density, which is more delocalized in A-DR1-T1 than in A-DR2-T1 (Fig. 8). In the maleimide moiety, the methyl substituent donates electron density so that a radical center is better stabilized at C3 than at C4. Likewise, in the alkene moiety, a radical center is less favorable at the terminal C1 atom than at the adjacent C2 atom where the substituents can donate electron density to C2.

Both effects combine to make A-DR1-T1 more stable than A-DR2-T1. The stability of the diradical intermediates is thus largely governed by the electron donor capabilities of the substituents at the radical centers. It decreases in the order DR1-T1 > DR3-T1 > DR4-T1 > DR2-T1, which is consistent with the spatial distribution of the spin density in the four diradical intermediates (Fig. 8).

T_1/S_0 Intersections

Since the second half reactions on paths DR1-DR4 are not feasible energetically, the system must return to the electronic ground state via intersystem crossing to complete the cyclization reaction in the S_0 state.[65,66] Such intersystem crossings occur preferentially close to intersections of the potential energy surfaces involved.

The most likely region for the $T_1 \rightarrow S_0$ intersystem crossing is near the diradical intermediates on paths DR1-DR4.[65,66] This is confirmed by our electronic structure computations. We located the corresponding T_1/S_0 crossing-point structures at the B3LYP-D3/6-31G*/PCM level (see ESI, Fig. S4). They are structurally and energetically very close to the related T_1 diradical intermediates and are thus easily accessible as long as the T_1 intermediates themselves can be reached. At these intersection structures the open-shell singlet and triplet states are degenerate, and the two unpaired

electrons are located on the two chemically unbound carbon atoms. The crossing-point structures are twisted (see ESI, Fig. S4), so there will be some covalent interaction between the radical centers leading to a nonzero (presumably small) spin-orbit coupling that mediates intersystem crossing.[65] After return to the S_0 state, an essentially barrierless ring closure of the singlet diradical leads to the formation of the closed-shell cyclic product (see Fig. 9).

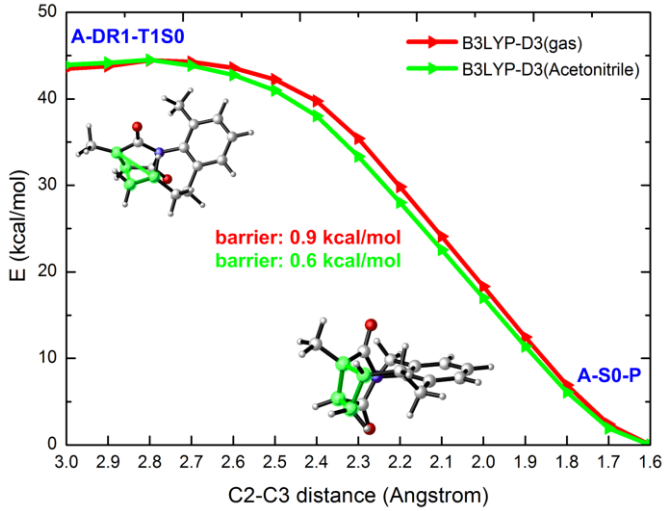

Fig. 9 B3LYP-D3/6-31G* (gas phase) and B3LYP-D3/6-31G*/PCM (acetonitrile solution) computed minimum-energy paths (MEPs) connecting the T_1/S_0 crossing point (A-DR1-T1S0) and the corresponding ground-state S_0 product (A-S0-P).

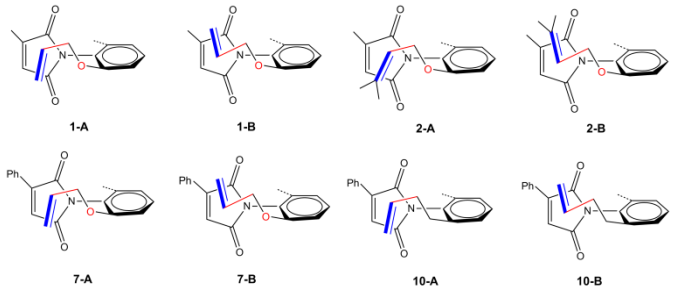

Fig. 10 Molecular structures used to study the effects of substituents at the maleimide double bond and the alkenyl tether. The compound indexes used here are the same as those used in the experimental work.[40] n-X stands for compound n with conformation X; for example, 9-A is compound 9 in conformation A.

Substituent Effects

The [2+2] photocyclization of atropisomeric maleimides is highly enantioselective experimentally, with more than 98% *ee*.[40] This is caused by the high barriers to rotation around the N-C(aryl) bond. For four maleimide substrates, measurements of the free energy barrier to rotation in toluene gave values of 31.6–31.7 kcal/mol.[40] The calculations for conformer A of our standard substrate (**1i**) yield barriers of 33.8 kcal/mol in the S_0 state and 19.7 kcal/mol in the T_1 state (see left panel of Fig. 3). Hence, because of these high barriers, racemization is blocked during the photoreaction, which leads to high enantiomeric excess in the photoproducts.

Experimentally, diastereomeric ratios (*dr*) were systematically studied for a series of atropisomeric maleimides with different substituents on the maleimide double bond and the alkenyl tether.[40] The *dr* values were not affected much by changing the link between the alkenyl tether and the N-aryl ring (cf. compound 1 vs. 9, O vs. CH2 link, 79:21 vs. 74:26) or by gem-dimethyl substitution at the terminal alkene carbon atom (cf. compound 1 vs. 2, 79:21 in both cases). By contrast, replacing the methyl substituent at the maleimide double bond (compounds 1 and 2) by a phenyl substituent (compounds 7 and 11) raises the *dr* value significantly to more than 99:1. To analyze the origin of this diastereoselectivity, we have performed additional computations on these compounds (see Fig. 10).

Table 1 Experimentally Measured Diastereomeric Ratios *dr* and Computed Differences (kcal/mol) in Free Energy Barriers $\Delta\Delta G^{\neq}_{DR1:DR3}$ and in Reaction Free Energies $\Delta\Delta G^{rx}_{DR1:DR3}$ between Paths DR1 and DR3 (C-C Bond Formation in the T_1 state). Compounds are Labeled as in Table 4 of the Experimental Work[40] and are Shown in Fig. 10.

Compound	1 (**1a**)	2 (**1b**)	7 (**1g**)	9 (**1i**)	10 (**1j**)
dr	79:21	79:21	>99:1	74:26	>99:1
$G^{\neq}_{DR1:DR3}$	-3.2	-3.0	-7.6	-1.3	-4.9
$G^{rx}_{DR1:DR3}$	-3.9	-4.9	-14.4	-2.3	-11.9

The *dr* value is the ratio of the yield of *exo* and *endo* photoproducts.[40] According to our calculations, they are formed separately via the DR1 and DR3 pathways (as shown before, the DR2 and DR4 pathways cannot compete with DR1 and DR3). Therefore, we computed the difference between the free energy barriers of the first half-reaction on paths DR1 and DR3 in the T_1 state ($\Delta\Delta G^{\neq}_{DR1:DR3}$) which is given by

$$G^{\neq}_{DR1:DR3} = \Delta G^{\neq}_{DR1} - \Delta G^{\neq}_{DR3}$$

with $G^{\neq}_{DR1} = G_{A-DR1-T1-TS1} - G_{A-T1-R}$ and $G^{\neq}_{DR3} = G_{B-DR3-T1-TS1} - G_{B-T1-R}$. The results are listed in Table 1. Evidently, compounds 1 and 2 have essentially the same $\Delta\Delta G_{DR1:DR3}{}^{\neq}$ and *dr* values. Compounds 7 and 10 have more negative $G_{DR1:DR3}{}^{\neq}$ values, hence path DR1 is more favored, and the *dr* values exceed 99:1. Analogously, compound 9 shows the opposite trend. Therefore, the more negative $\Delta\Delta G^{\neq}_{DR1:DR3}$, the larger is the *dr* value.

According to the Bell-Evans-Polanyi principle, one may expect a correlation between barrier heights and reaction energies for analogous reactions in related systems: barriers decrease when the reaction becomes more exothermic. Having this in mind, we also computed the corresponding differences in the reaction free energies on the DR1 and DR3 pathways ($\Delta\Delta G^{rx}_{DR1:DR3}$) given by

$$G^{rx}_{DR1:DR3} = \Delta G^{rx}_{DR1} - \Delta G^{rx}_{DR3}$$

with $\Delta G^{rx}_{DR1} = G_{A-DR1-T1} - G_{A-T1-R}$ and $G^{rx}_{DR3} = G_{B-DR3-T1} - G_{B-T1-R}$. The results are included in Table 1. As expected, they are analogous to those for the barriers, and the trends are even more pronounced: phenyl substitution at the maleimide double bond (compounds 7 and 10) makes the DR1 pathway much more favorable thermodynamically.

This can be understood by considering the electronic structures of the triplet diradical intermediates (e.g. A-DR1-T1 and B-DR3-T1). Fig. S11 shows the computed spin density distributions in these intermediates for compounds 1, 2, 7, and 10 (see ESI for further discussion). In these compounds, the diastereoselectivity is thus ultimately governed by the ability of the substituents to stabilize the intermediate diradical triplet species.

Comparison with other Functionals

All preceding results were obtained at the B3LYP-D3/6-31G*/PCM level. To check their sensitivity with regard to the choice of exchange-correlation functional, we performed single-point DFT/6-31G*/PCM calculations on the optimized B3LYP-D3/6-31G*/PCM geometries using the range-separated hybrid functional CAM-B3LYP, the global hybrid functional PBE0, and the global hybrid meta-GGA functional M06-2X, with inclusion of Grimme dispersion corrections (D3) in the case of CAM-B3LYP and PBE0. Fig. 11 compares the corresponding T_1 energy profiles for pathways DR1 and DR2 of our standard substrate (**1i**) with those obtained at the B3LYP-D3 level. Evidently, all functionals yield qualitatively similar profiles. On pathway DR1, the first half-reaction is very facile and leads to a fairly stable triplet intermediate. Pathway DR2 is confirmed to be less favorable by a significant margin in all cases. On a quantitative scale, the three single-point energy profiles generally lie somewhat below the B3LYP-D3 profile, both for DR1 and DR2 (e.g. by about 7–8 kcal/mol in the case of the intermediate), but this does not affect any of the mechanistic conclusions.

Importantly, the different functionals also predict qualitatively the same path selectivity. This can be seen from the computed differences in energy barriers and reaction energies between pathways DR1 and DR2 of our standard substrate (1i), see Table 2. Obviously, all functionals give similar values for these energy differences, with minor deviations up to 2.9 kcal/mol for the first barrier and less than 1.6 kcal/mol for the reaction energy.

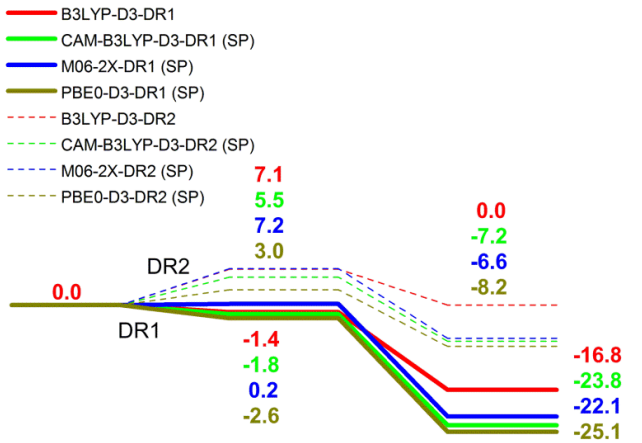

Fig. 11 Single-point energies from CAM-B3LYP-D3, M06-2X, and PBE0-D3 calculations on the B3LYP-D3 optimized geometries for pathways DR1 and DR2 (see text). The T_1 reactant serves as reference point in each potential energy profile. See Supporting Information for the other pathways DR3-DR8.

Table 2 Computed Differences (kcal/mol) in Energy Barriers $\Delta\Delta E^{\neq}_{DR1:DR2}$ and in Reaction Energies $\Delta\Delta E^{rx}_{DR1:DR2}$ between Paths DR1 and DR2 Computed by Different Exchange-Correlation Functionals (B3LYP-D3, CAM-3LYP-D3, M06-2X, and PBE0-D3). See Fig. 11 for the Associated Potential Energy Profiles and the Supporting Information for the Results for Pathways DR3-DR8.

	First half reaction	
	$E^{\neq}_{DR1:DR2}$	$E^{rx}_{DR1:DR2}$
B3LYP-D3	-8.5	-16.8
CAM-B3LYP-D3	-7.3	-16.6
M06-2X	-7.0	-15.5
PBE0-D3	-5.6	-16.9

Comparison with Experiment

In the experimental work,[40] the photocyclization of the atropisomeric maleimides was shown to proceed via the T_1 state: formation of the first CC bond yields a triplet diradical intermediate, which then undergoes intersystem crossing to the singlet ground state, with subsequent formation of the second CC bond. Our present calculations confirm this nonadiabatic photocyclization mechanism and provide additional structural and energetic information, by focusing on two conceivable reactions paths (DR1-DR4) for two possible conformers (A and B) of a prototypical substrate (**1i**) and by identifying all relevant minima and transition states as well as T_1/S_0 intersection structures.

Experimentally, scrambling studies were performed on atropisomeric maleimides that are mono-substituted at the terminal alkene carbon to explore the initial bond-forming process.[40] Two plausible scenarios were proposed to explain the observed lack of scrambling in the alkene moiety, namely either a preference of DR1 over DR2 or a higher cyclization rate of DR2.[40] Our current DFT calculations clearly favor the first alternative since the computed free-energy barrier for the initial CC bond formation in the triplet state is much lower for DR1 than for DR2 (1.5 vs. 9.7 kcal/mol). The electronic structure calculations offer two explanations for the preference of DR1 over DR2: the relevant transition state for the initial CC bond formation benefits from more favorable electrostatic interactions between the two polarized C=C double bonds for DR1 compared with DR2, and the formed triplet diradical intermediate is better stabilized in the case of DR2 through substituent effects.

In the experimental work, the observed high enantioselectivity of the photocyclization was ascribed to high rotation barriers around the N-C(aryl) bond; values of more than 30 kcal/mol were measured for the ground-state barriers in toluene.[40] The DFT calculations confirm this explanation: for our standard substrate they yield rotation barriers of around 34 kcal/mol in the S_0 state and around 20 kcal/mol in the T_1 state. Thus they predict conformational stability also in the triplet state, which is essential for achieving high enantioselectivity by preventing racemization during the T_1 photoreaction.

Experimentally, the photocyclization of atropisomeric maleimides generally leads to two diastereomeric photoproducts, the major *exo* and the minor *endo* form.[40] They are accessible via the DR1 and DR3 pathways, respectively. The diastereomeric ratio *dr* depends significantly on the substituents on the maleimide double bond, whereas the group linking the alkenyl tether and the N-aryl ring has little effect.[40] The observed *dr* values for a set of five substrates correlate well with the computed differences in the T_1 free-energy barriers for the initial CC bond formation on pathways DR1 and DR3, and also with the corresponding T_1 reaction free energies (i.e. with the stability of the formed triplet diradical intermediates). Specifically, we find that phenyl substitution on the maleimide double bond is capable of selectively stabilizing radical centers in these intermediates and thus enhancing the *dr* value in such compunds. According to this analysis, the diastereoselectivity is thus ultimately governed by the ability of the substituents to stabilize the triplet diradical intermediates.

Conclusions

In summary, we have computationally studied the reaction mechanism of the [2+2] photocycloaddition of atropisomeric maleimides.[40] We explored eight nonadiabatic photocycloaddition pathways that lead to distinct regioisomeric photoproducts. These photocyclizations proceed in a stepwise manner: the first CC bond is formed adiabatically in the T_1 state with a very small barrier, followed by an intersystem crossing to the S_0 state and an

essentially barrierless formation of the second CC bond in the ground state. Our electronic structure calculations shed light on the origin of the observed regio-, enantio-, and diastereoselectivity of this photoreaction and offer explanations for the observed substituent effects on enantioselectivity (*ee*) and diastereoselectivity (*dr*). The computational results are consistent with the available experimental findings and confirm the basic mechanism proposed in the experimental work,[40] while providing additional detailed insight at the atomistic level. Finally, we hope that the present study may motivate further computational research on stereocontrol of photoreactions that may provide complementary access to molecules with unique stereochemical and structural complexity.[67,68]

Acknowledgments

This work was supported by the National Natural Science Foundation of China (No. 21522302 and 21520102005); G.C. is also grateful for financial support from "Recruitment Program of Global Youth Experts" and "Fundamental Research Funds for Central Universities".

References

1 I. Ojima, *Catalytic Asymmetric Synthesis*. John Wiley & Sons, 2004.
2 E. Juaristi and V.A. Soloshonok, *Enantioselective Synthesis of Beta-Amino Acids*. John Wiley & Sons, 2005.
3 A. Berkessel and H. Gröger, *Asymmetric Organocatalysis: from Biomimetic Concepts to Applications in Asymmetric Synthesis*. John Wiley & Sons, 2006.
4 J. Morrison, *Asymmetric Synthesis*. Elsevier, 2012.
5 R.E. Gawley and J. Aubé, *Principles of Asymmetric Synthesis*. Elsevier, 2012.
6 B. List, R.A. Lerner, and C.F. Barbas, *J. Am. Chem. Soc.*, 2000, **122**, 2395–2396.
7 K.A. Ahrendt, C.J. Borths, and D.W.C. MacMillan, *J. Am. Chem. Soc.*, 2000, **122**, 4243–4244.
8 W. Notz and B. List, *J. Am. Chem. Soc.*, 2000, **122**, 7386–7387.
9 M. Rueping, A.P. Antonchick, and T. Theissmann, *Angew. Chem. Int. Ed.*, 2006, **45**, 3683–3686.
10 T.D. Beeson, A. Mastracchio, J.-B. Hong, K. Ashton, and D.W.C. MacMillan, *Science*, 2007, **316**, 582–585.
11 K. Gopalaiah, *Chem. Rev.*, 2013, **113**, 3248–3296.
12 J.E. Spangler and H.M.L Davies, *J. Am. Chem. Soc.,* 2013, **135**, 6802–6805.
13 M. Uyanik, H. Hayashi, and K. Ishihara, *Science*, 2014, **345**, 291–294.
14 K.C.W Chong, J. Sivaguru, T. Shichi, Y. Yoshimi, V. Ramamurthy, and J.R. Scheffer, *J. Am. Chem. Soc.*, 2002, **124**, 2858–2859.
15 Y. Inoue and V. Ramamurthy, *Chiral Photochemistry*. CRC Press, 2004.
16 A. Bauer, F. Westkämper, S. Grimme, and T. Bach, *Nature*, 2005, **436**(7054), 1139–1140.
17 S. Lerch, L.-N. Unkel, and M. Brasholz, *Angew. Chem. Int. Ed.*, 2014, **53**, 6558–6562.
18 R. Brimioulle, A. Bauer, and T. Bach, *J. Am. Chem. Soc.*, 2015, **137**, 5170–5176.
19 N.J. Turro, *Modern Molecular Photochemistry*. University Science Books, 1991.
20 N.J. Turro, V. Ramamurthy, and J.C. Scaiano, *Principles of Molecular Photochemistry: An Introduction*. University science books, 2009.
21 J.N. Gamlin, R. Jones, M. Leibovitch, B. Patrick, J.R. Scheffer, and J. Trotter, *Acc. Chem. Res.*, 1996, **29**, 203–209.
22 T. Bach, H. Bergmann, B. Grosch, and K. Harms, *J. Am. Chem. Soc.,* 2002, **124**, 7982–7990.
23 M.A. Garcia-Garibay, *Acc. Chem. Res.*, 2003, **36**, 491–498.
24 J. Sivaguru, A. Natarajan, L.S. Kaanumalle, J. Shailaja, S. Uppili, A. Joy, and V. Ramamurthy, *Acc. Chem. Res.*, 2003, **36**, 509–521.
25 T. Mori, R.G. Weiss, and Y. Inoue, *J. Am. Chem. Soc.*, 2004, **126**, 8961–8975.
26 C. Yang, T. Mori, Y. Origane, Y.H. Ko, N. Selvapalam, K. Kim, and Y. Inoue, *J. Am. Chem. Soc.*, 2008, **130**, 8574–8575.
27 N. Vallavoju, S. Selvakumar, S. Jockusch, M.P. Sibi, and J. Sivaguru, *Angew. Chem. Int. Ed.*, 2014, **53**, 5604–5608.
28 J. Clayden, *Angew. Chem. Int. Ed.*, 1997, **36**, 949–951.
29 A. Ates and D.P. Curran, *J. Am. Chem. Soc.*, 2001, **123**, 5130–5131.
30 J. Clayden, *Chem. Comm.*, 2004, pages 127–135.
31 D. Campolo, S. Gastaldi, C. Roussel, M.P. Bertrand, and M. Nechab, *Chem. Soc. Rev.*, 2013, **42**, 8434–8466.
32 A.J.-L. Ayitou and J. Sivaguru, *J. Am. Chem. Soc.*, 2009, **131**, 5036–5037.
33 A.J.-L. Ayitou, J.L. Jesuraj, N. Barooah, A. Ugrinov, and J. Sivaguru, *J. Am. Chem. Soc.*, 2009, **131**, 11314–11315.
34 J.L. Jesuraj and J. Sivaguru, *Chem. Commun.*, 2010, **46**, 4791–4793.
35 N.N.B. Kumar, O.A.Mukhina, and A.G. Kutateladze, *J. Am. Chem. Soc.*, 2013, **135**, 9608–9611.
36 R. Raghunathan, E. Kumarasamy, A. Iyer, A. Ugrinov, and J. Sivaguru, *Chem. Commun.*, 2013, **49**, 8713–8715.
37 A.J.-L. Ayitou, G. Fukuhara, E. Kumarasamy, Y. Inoue, and J. Sivaguru, *Chem. Eur. J.*, 2013, **19**, 4327–4334.
38 E. Kumarasamy and J. Sivaguru, *Chem. Commun.*, 2013, **49**, 4346–4348.
39 A.J.-L. Ayitou, A. Clay, E. Kumarasamy, S. Jockusch, and J. Sivaguru, *Photochem. Photobiol. Sci.*, 2014. **13**, 141–44.
40 E. Kumarasamy, R. Raghunathan, S. Jockusch, A. Ugrinov, and J. Sivaguru, *J. Am. Chem. Soc.*, 2014, **136**, 8729–8737.
41 P. H.-Y. Cheong, C. Y. Legault, J. M. Um, N. Celebi-Ölcüm, and K. N. Houk, *Chem. Rev.*, 2011, **111**, 5042–5137.
42 E. H. Krenske and K. N. Houk, *Acc. Chem. Res.*, 2013, **46**, 979–989.
43 J. N. Harvey, *WIREs Comput. Mol. Sci.*, 2014, **4**, 1–14.
44 M. R. A. Blomberg, T. Borowski, F. Himo, R.-Z. Liao, and P. E. M. Siegbahn, *Chem. Rev.*, 2014, **114**, 3601–3658.
45 W. Thiel, *Angew. Chem. Int. Ed.*, 2014, **53**, 8605–8613.
46 G.-J. Cheng, X. H. Zhang, L. W. Chung, L. P. Xu, and Y.-D. Wu, *J. Am. Chem. Soc.*, 2015, **137**, 1706–1725.
47 R. G. Parr and W. T. Yang, *Density-Functional Theory of Atoms and Molecules*. Oxford University Press, USA, 1994.
48 S. H. Vosko, L. Wilk, and M. Nusair, *Can. J. Phys.*, 1980, **58**, 1200–1211.
49 A. D. Becke, *Phys. Rev. A*, 1988, **38**, 3098–3100.
50 C. Lee, W. T. Yang, and R. G. Parr, *Phys. Rev. B*, 1988, **37**, 785–789.
51 A. D. Becke, *J. Chem. Phys.*, 1993, **98**, 1372–1377.
52 Y. Zhao and D. G. Truhlar, *Theor. Chem. Acc.*, 2008, **120**, 215–241.
53 J.P. Perdew and M. Burke, K. Ernzerhof, *Phys. Rev. Lett.*, 1996, **77**, 3865–3868.
54 T. Yanai, D. P. Tew, and N. C. Handy, *Chem. Phys. Lett.*, 2004, **393**, 51–57.

55 R. Ditchfield, W. J. Hehre, and J. A. Pople, *J. Chem. Phys.*, 1971, **54**, 724–728.
56 P. C. Hariharan and J. A. Pople, *Theor. Chem. Acc.*, 1973, **28**, 213–222.
57 V. Barone and M. Cossi, *J. Phys. Chem. A*, 1998, **102**, 1995–2001.
58 S. Grimme, J. Antony, S. Ehrlich, and H. Krieg, *J. Chem. Phys.*, 2010, **132**, 154104.
59 M. J. Frisch, G. W. Trucks, H. B. Schlegel, G. E. Scuseria, M. A. Robb, J. R. Cheesem, G. Scalmani, V. Barone, B. Mennucci, G. A. Petersson, H. Nakatsuji, M. Caricato, X. Li, H. P. Hratchian, A. F. Izmaylov, J. Bloino, G. Zheng, J. L. Sonnenberg,M. Hada,M. Ehara, K. Toyota, R. Fukuda, J. Hasegawa, M. Ishida, T. Nakajima, Y. Honda, O. Kitao, H. Nakai, T. Vreven, J. A. Montgomery Jr., J. E. Peralta, F. Ogliaro, M. Bearpark, J. J. Heyd, E. Brothers, K. N. Kudin, V. N. Staroverov, R. Kobayashi, J. Normand, K. Raghavachari, A. Rendell, J. C. Burant, S. S. Iyengar, J. Tomasi, M. Cossi, N. Rega, J. M. Millam,M. Klene, J. E. Knox, J. B. Cross, V. Bakken, C. Adamo, J. Jaramillo, R. Gomperts, R. E. Stratmann, O. Yazyev, A. J. Austin, R. Cammi, C. Pomelli, J. W. Ochterski, R. L. Martin, K. Morokuma, V. G. Zakrzewski, G. A. Voth, P. Salvador, J. J. Dannenberg, S. Dapprich, A. D. Daniels, Ö. Farkas, J. B. Foresman, J. V. Ortiz, J. Cioslowski, and D. J. Fox, *Gaussian 09, Revision A.02. Gaussian, Inc.,* Wallingford CT, 2009.
60 C. Ciminelli, G. Granucci, and M. Persico, *Chemistry-A European Journal*, 2004, **10**, 2327–2341.
61 J. Kästner, J.M. Carr, T.W. Keal, W. Thiel, A. Wander, and P. Sherwood, *J. Phys. Chem. A*, 2009, **113**, 11856–11865.
62 ChemShell3.5, a Computational Chemistry Shell, see www.chemshell.org.
63 G.L. Cui and W. Thiel, *J. Phys. Chem. Lett.*, 2014, **5**, 2682–2687.
64 X.-P. Chang, G.L. Cui, W.-H. Fang, and W. Thiel, *ChemPhysChem*, 2015, **16**, 933–937.
65 J. Michl, *J. Am. Chem. Soc.,* 1996, **118***,* 3568-3579.
66 A.G. Kutateladze and W. A. McHale, Jr., *Arkivoc*, 2005 (iv), 88-101.
67 R. Brimioulle, D. Lenhart, M. M. Maturi, and T. Bach, *Angew. Chem. Int. Ed.*, 2015, **54**, 3872–3890.
68 E. Kumarasamy, R. Raghunathan, M. P. Sibi, and J. Sivaguru, *Chem. Rev.*, 2015, **115**, 11239–11300.